2-13-2023

Scaling of Turbulence and Microphysics in a Convection–Cloud Chamber of Varying Height

Subin Thomas
Michigan Technological University, subint@mtu.edu

Fan Yang
Brookhaven National Laboratory

Mikhail Ovchinnikov
Pacific Northwest National Laboratory

Will Cantrell
Michigan Technological University, cantrell@mtu.edu

Raymond Shaw
Michigan Technological University, rashaw@mtu.edu

AGU ADVANCING EARTH AND SPACE SCIENCE

JAMES | Journal of Advances in Modeling Earth Systems®

RESEARCH ARTICLE
10.1029/2022MS003304

Key Points:

- Increasing the height of a convection-cloud chamber leads to an increase in characteristic velocity and time scales
- Cloud droplet size distributions can be approximately matched by increasing the total aerosol injection rate as the square of the height
- Concentration of large cloud droplets due to collision and coalescence increases monotonically with increasing height

Correspondence to:
R. A. Shaw,
rashaw@mtu.edu

Citation:
Thomas, S., Yang, F., Ovchinnikov, M., Cantrell, W., & Shaw, R. A. (2023). Scaling of turbulence and microphysics in a convection–cloud chamber of varying height. *Journal of Advances in Modeling Earth Systems*, *15*, e2022MS003304. https://doi.org/10.1029/2022MS003304

Received 15 JUL 2022
Accepted 26 JAN 2023

Author Contributions:
Conceptualization: Raymond A. Shaw
Formal analysis: Subin Thomas
Investigation: Subin Thomas, Fan Yang, Mikhail Ovchinnikov, Will Cantrell, Raymond A. Shaw
Software: Subin Thomas, Fan Yang, Mikhail Ovchinnikov
Supervision: Raymond A. Shaw
Writing – original draft: Subin Thomas, Raymond A. Shaw
Writing – review & editing: Subin Thomas, Fan Yang, Mikhail Ovchinnikov, Will Cantrell, Raymond A. Shaw

Scaling of Turbulence and Microphysics in a Convection–Cloud Chamber of Varying Height

Subin Thomas[1], Fan Yang[2], Mikhail Ovchinnikov[3], Will Cantrell[1], and Raymond A. Shaw[1]

[1]Michigan Technological University, Houghton, MI, USA, [2]Brookhaven National Laboratory, Upton, NY, USA, [3]Pacific Northwest National Laboratory, Richland, WA, USA

Abstract The convection–cloud chamber enables measurement of aerosol and cloud microphysics, as well as their interactions, within a turbulent environment under steady-state conditions. Increasing the size of a convection–cloud chamber, while holding the imposed temperature difference constant, leads to increased Rayleigh, Reynolds and Nusselt numbers. Large–eddy simulation coupled with a bin microphysics model allows the influence of increased velocity, time, and spatial scales on cloud microphysical properties to be explored. Simulations of a convection–cloud chamber, with fixed aspect ratio and increasing heights of $H = 1$, 2, 4, and (for dry conditions only) 8 m are performed. The key findings are: Velocity fluctuations scale as $H^{1/3}$, consistent with the Deardorff expression for convective velocity, and implying that the turbulence correlation time scales as $H^{2/3}$. Temperature and other scalar fluctuations scale as $H^{-3/7}$. Droplet size distributions from chambers of different sizes can be matched by adjusting the total aerosol injection rate as the horizontal cross-sectional area (i.e., as H^2 for constant aspect ratio). Injection of aerosols at a point versus distributed throughout the volume makes no difference for polluted conditions, but can lead to cloud droplet size distribution broadening in clean conditions. Cloud droplet growth by collision and coalescence leads to a broader right tail of the distribution compared to condensation growth alone, and this tail increases in magnitude and extent monotonically as the increase of chamber height. These results also have implications for scaling within turbulent, cloudy mixed-layers in the atmosphere, such as fog layers.

Plain Language Summary In a convection–cloud chamber, turbulent convection is generated by heating the bottom surface and cooling the top surface. Water-supersaturated conditions are achieved by maintaining the bottom and top surfaces wet. When aerosols are injected into the resulting turbulent, supersaturated flow, cloud droplets are formed and grow by vapor condensation, and possibly by collision and coalescence. The relative roles of condensation due to mean properties and fluctuating properties, as well as the role of collisional growth, depend on the time and velocity scales of the turbulence, all of which depend on the height of the chamber. In this work, turbulence and cloud properties in a convection–cloud chamber are simulated for several chamber heights. It is found that time and velocity scales increase with chamber height; cloud droplet size distributions can be approximately matched by appropriately increasing the aerosol injection rate; and the relevance of collisional growth increases with chamber height. These findings will help guide future computational and laboratory implementations of cloud formation in thermal, moist convection.

1. Introduction

The Pi Chamber is a laboratory convection—cloud chamber in which "fully resolved" by nature aerosol and cloud microphysical processes take place within a turbulent medium (Chang et al., 2016). This is a fundamentally different approach than the traditional expansion cloud chamber, which takes its inspiration from the parcel viewpoint, that is, all particles are exposed to the same environment and have the same lifetime. In contrast, a convection—cloud chamber is inspired by a turbulent mixed-layer viewpoint, in which microphysical processes exist in a dynamic steady state with aerosols being continuously introduced, and cloud droplets settling to the bottom. The aerosols and cloud particles are exposed to fluctuating velocity, temperature and water vapor fields, resulting in both positive and negative supersaturations, leading to corresponding activation and deactivation of cloud condensation nuclei (MacMillan et al., 2022; Prabhakaran et al., 2020), as well as the growth and evaporation of cloud droplets (Chandrakar et al., 2016) and ice particles (Desai et al., 2019).

The Pi Chamber volume is a cylinder with height and radius both equal to 1 m (the name denoting the volume of π m^3). The thermodynamic conditions in a convection–cloud chamber, including the supersaturation forcing

analogous to the updraft strength in a rising parcel, depend on the boundary conditions, including the temperature difference ΔT between top and bottom surfaces. For a given ΔT, the chamber height H determines the intensity of the turbulence, and the corresponding range of length and time scales, as well as the strength of scalar fluctuations, to which aerosol and cloud particles are exposed. For several reasons, it is of interest to achieve a broader range of length and time scales in a convection—cloud chamber. An increase in the Lagrangian correlation time for scalar fluctuations is relevant to turbulence-induced broadening of the droplet size distribution (Cooper, 1989). An increase in the root-mean-square velocity scale will allow larger particles to exist in the volume, thereby interacting with other aerosols and droplets for an extended time. An increase in the lifetime of aerosols and droplets in the chamber will allow for a wider range of chemical transformations and aerosol processing to occur (Bhandari et al., 2019). And finally, we expect that an increase in the lifetime of cloud droplets and ice crystals should lead to enhanced probability of experiencing collisional growth. In this paper we explore how turbulence and microphysical properties scale with the height of a convection—cloud chamber using large eddy simulations.

The Pi Chamber produces fluid turbulence via Rayleigh–Bénard convection (RBC), and subsequently the dominant spatial and temporal scales present within the system depend on attainable Reynolds numbers. This Reynolds number depends on the Rayleigh number and Prandtl number (Chillà & Schumacher, 2012; Thomas et al., 2022). In a convection chamber, for high Reynolds numbers, a larger range of spatial and temporal scales can be accessed by reducing the Prandtl number, or increasing the Rayleigh number. The Prandtl number is fixed by selecting a convecting fluid. Similarly for a fixed geometry (as well as fixed fluid properties and gravitational acceleration), the Rayleigh numbers depends only on the temperature difference between the top and bottom surfaces. Thus for the Pi Chamber with a fixed geometry, and a selected convecting fluid, only about 2 orders of magnitude of Rayleigh numbers (i.e., 10^8–10^{10}) can be explored (Chang et al., 2016). Furthermore, decoupling the Rayleigh number from the thermodynamic forcing requires altering the water vapor boundary conditions, for example, by using salt solutions (Shawon et al., 2021). In practice the Rayleigh number ranges explored have been limited to about 1 order of magnitude due to experimental limitations (Niedermeier et al., 2018).

The Rayleigh numbers ranges explored by the Michigan Tech Pi cloud chamber are on the order of 10^9. In contrast, the atmospheric Rayleigh number is $\mathcal{O}\left(10^{21}\right)$ (Vallis et al., 2019), which is unattainable in the laboratory (except perhaps for superfluid convection (Niemela et al., 2000)). From the definition of Rayleigh number (Equation 1 in Section 2), $Ra \propto H^3 \Delta T$. For the same temperature difference, the atmospheric length scales are 1,000 times that of the cloud chamber. Hence, it is necessary to scale the results of aerosol-cloud-turbulence interactions (Bhandari et al., 2019; Chandrakar et al., 2018; Prabhakaran et al., 2020; Shawon et al., 2021) from cloud chamber to the atmosphere. To be clear, the goal in the laboratory is not to match Ra and Re in the atmosphere, which is likely impossible, but rather to explore atmospherically-relevant ranges of microphysical dimensionless numbers. Non-dimensionalizing the microphysical equations for RBC (Thomas et al., 2022), suggests that the following variables are of relevance: water vapor supersaturation (the ratio of the water vapor mixing ratio to the saturation mixing ratio minus 1), the Damkoehler number (the ratio of the turbulent mixing time scale to the time scale for droplet growth, i.e., phase relaxation time), and Rouse or sedimentation number (the ratio of the droplet terminal speed to the characteristic velocity scale for the turbulence). In addition, we can speculate that for the growth of cloud droplets by collision and coalescence, a relevant dimensionless parameter would be akin to a Knudsen number, consisting of the ratio of the collision mean-free path and the chamber dimension H. Thus, our attention here is focused on scaling of turbulence times and velocities, as well as collision growth within a convection—cloud chamber of varying height.

The potential of using a large cloud chamber research facility to explore key scientific questions relevant to weather and climate were discussed at a recent workshop held at the National Center for Atmospheric Research in 2019, and the consensus was that a significant number of atmospherically relevant chemical and physical processes could be effectively studied in a chamber with characteristic dimension of order 10 m in size (Shaw et al., 2020). Apart from the development of new experimental approaches and improved instrumentation, the need for advancement of computational models validated against the experiments also emerged as an important science priority from the workshop. In this paper, we focus on the growth of cloud droplets by collision—coalescence to illustrate the scaling with chamber height, because of its importance for precipitation growth and aerosol processing in the atmosphere (Kang et al., 2022). Evidence for efficient collision-coalescence has not yet been observed in the Michigan-Tech Pi cloud chamber limited by its height of 1 m (Chandrakar et al., 2016; Thomas et al., 2019). The distances traveled by droplets before they precipitate out increases with H, and thus increasing the height of a chamber should also increase the probability of cloud droplet growth by collision-coalescence.

Thus, the current study is a first step to explore the effect of cloud chamber height on turbulence dynamics and cloud microphysics. To that effect, we scale the existing cloud chamber simulation setup discussed in Thomas et al. (2019) to larger sizes, while maintaining the same aspect ratio as the Pi Chamber. These large eddy simulation (LES) results for chambers of different sizes illustrate and validate the scaling of temperature fluctuations, the scaling of characteristic velocity, and changes in microphysical interactions with height. The current article is divided into the following sections. Section 2 explores the scaling of the non-dimensional parameter space, and specifically the effect of scaling on velocities, mean and fluctuating scalars. In Section 3, the details of the numerical modeling of convection–cloud chambers of different sizes are described. In Section 4, the results are presented and discussed and finally in Section 5, we discuss the further studies and present our concluding remarks.

2. Scaling of Variables

A description of a convection–cloud chamber relies on two independently developed knowledge bases: Rayleigh-Bénard convection and cloud microphysics. For historical reasons, the theoretical development of RBC has used non–dimensional numbers. It has been less common, but is also possible to express non–dimensional numbers to study the condensational growth processes (Thomas et al., 2022). Using the widely accepted findings from the RBC and cloud microphysics communities, we can obtain a starting understanding of the effect of scaling the height of a convection–cloud chamber. This approach implicitly assumes that the RBC and cloud microphysical processes are independent. Later, in the LES analysis, the processes are fully coupled.

The characteristic length scale is the height of the cloud chamber(H) for the moist RBC. The characteristic non-dimensional numbers are Rayleigh number (Ra), Nusselt number (Nu), Prandtl number (Pr), Schmidt number (Sc) and Lewis number (Le) for a moist RBC system (Thomas et al., 2022). Ra and Nu describe the dynamics of the system. Pr, Sc, and Le describe the convecting fluid properties, including momentum diffusivity (ν), thermal diffusivity(α) and water vapor diffusivity(ν_v). These diffusivities have weak thermal dependence and hence are assumed constant for the temperature range explored; consequently Pr, Sc, Le are taken as constants. Finally, Reynolds number (Re) and Nusselt number (Nu) have a weak dependence on the aspect ratio of the cloud chamber (Hartmann et al., 2021), hence the aspect ratio is maintained constant across different sizes to allow for fair comparison.

As mentioned in the previous section, the microphysical dimensionless variables are supersaturation (s), Damkoehler number (Da), and Rouse number (Rou). When fluctuations are considered, the magnitude of the standard deviation to the mean is also relevant, for example, $\sigma_T/\overline{T}$, $\sigma_{q_v}/\overline{q_v}$, and $\sigma_s/\overline{s}$. The scaling of these dimensionless variables requires a knowledge of how characteristic turbulence time and velocity, as well as scalar fluctuations (temperature, water vapor, supersaturation), vary with chamber dimension H. These will be considered below.

2.1. Rayleigh Number

The Rayleigh number is defined as the ratio between the product of buoyancy forces and heat advection to the product of viscous and heat conduction in a fluid (Chillà & Schumacher, 2012). It is defined as

$$Ra = \frac{g\,\beta\,H^3\,\Delta T}{\nu\,\alpha}, \tag{1}$$

where g is the gravitational acceleration and β is the coefficient of thermal expansion. Therefore with constant fluid properties and g, Rayleigh number scales as

$$Ra \propto H^3 \Delta T. \tag{2}$$

A larger Rayleigh number corresponds to a stronger turbulent flow and more efficient convective heat transfer. From Equation 2, to increase an order of magnitude of Ra, H needs to be increased by only a factor of 2.15, in contrast to increasing the ΔT by factor of 10.

2.2. Nusselt Number

The Nusselt number is the ratio of actual heat transferred to that of heat transferred by pure conduction. Hence, Nusselt number represents the non-dimensional heat transfer in a dry RBC flow. For moist and cloudy RBC systems, the Nusselt number can be written as (Thomas et al., 2022; Zhang et al., 2019),

$$\mathrm{Nu}_{\mu} = \frac{\overline{w'T'} + \frac{L}{C_p}\overline{w'Q'_v} - \alpha\nabla_z\overline{T} - \frac{L}{C_p}\nu_v\nabla_z\overline{Q_v}}{\alpha\frac{\Delta T}{H} + \nu_v\frac{L}{C_p}\frac{\Delta Q_v}{H}}, \tag{3}$$

where L is the latent heat of water vapor condensation and C_p is specific heat capacity of air at constant pressure. Also, the prime (indicated by $'$) quantities are the deviations from the mean (indicated by overbar). For a dry RBC system (for $Ra < 10^{17}$ with solid top and bottom boundaries), it has been demonstrated experimentally (Niemela et al., 2000) and numerically (Iyer et al., 2020) that Nusselt number has a Rayleigh number dependence given by

$$Nu \propto Ra^{1/3} \propto H\Delta T^{1/3}. \tag{4}$$

Therefore, in order to double the Nusselt number, either H has to be doubled or ΔT increased by 8 times.

Based on Equations 3 and 4, the total heat flux scales (i.e., numerator in Nu) as

$$\overline{w'T'} + \frac{L}{C_p}\overline{w'Q'_v} - \alpha\nabla_z\overline{T} - \frac{L}{C_p}\nu_v\nabla_z\overline{Q_v} \propto H^0. \tag{5}$$

In other words, the total heat flux is independent of the height of the chamber, and is dictated by the temperature and water vapor boundary conditions.

2.3. Characteristic Velocity

Scaling of the characteristic turbulence velocity is important to consider because it enters dimensionless parameters such as the Rouse number. The free-fall velocity is traditionally used as the characteristic velocity scale for RBC (Chillà & Schumacher, 2012). This free fall velocity scale is given by

$$w = (g\,H\,\beta\Delta T)^{1/2} \propto (H\,\Delta T)^{1/2} \tag{6}$$

An alternative candidate is the convective velocity scale introduced by Deardorff (1970) and is given by

$$w^* = \left(\frac{g}{T}z_i\overline{wT}_0\right)^{1/3}. \tag{7}$$

For RBC, $z_i = H$ and $\overline{wT}_0$ is the kinematic heat flux near the surface. Also, it should be noted that $\overline{wT}_0$ is independent of H. Therefore, the Deardorff velocity scale can be shown to vary with height as

$$w^* \propto H^{1/3}. \tag{8}$$

2.4. Characteristic Time Scale

The turbulence time scale enters dimensionless parameters such as the Damkoehler number. Since the characteristic length scale of RBC is H, the characteristic time scale depends on the choice of characteristic velocity scale. Hence, for a free fall velocity scale given by Equation 6 and constant ΔT,

$$\tau \propto H^{1/2}\Delta T^{-1/2} \propto H^{1/2}. \tag{9}$$

The second proportionality presumably holds if Nusselt number scales as $Ra^{1/3}$, since that implies that the thermal energy flux is limited by the viscous boundary layer and is independent of H. Hence according to Equation 9, the time scale increases as the height of the chamber H increases, but can be counteracted by increasing the temperature difference between the top and bottom surfaces ΔT.

For the Deardorff velocity scale given by Equation 8,

$$\tau \propto H^{2/3}, \tag{10}$$

for constant ΔT. Again, we have assumed that the turbulent heat flux is independent of H, as suggested by Equations 4 and 5.

2.5. Mean Temperature and Water Vapor Mixing Ratio

The volume-averaged mean temperature and mean water vapor mixing ratio are given by

$$\bar{T} = \frac{\rho_b T_b + \rho_t T_t}{\rho_b + \rho_t} \tag{11}$$

and

$$\bar{Q} = \frac{\rho_b Q_{sat}(T_b) + \rho_t Q_{sat}(T_t)}{\rho_b + \rho_t}, \tag{12}$$

where ρ_t and ρ_b are the densities of the fluid at the top and the bottom of the chamber, respectively. In Equations 11 and 12, we assume efficient mixing and ignore the effects of the sidewalls. The equations also assume, parcels of equal volume from the top and bottom plates mix together in the bulk. Hence, the density terms have to be accounted for. The effect of sidewalls is discussed in detail in Thomas et al. (2019). Similarly, for any passive scalar the volume averaged mean is written as

$$\overline{\Psi} = \frac{\rho_b \Psi_b + \rho_t \Psi_t}{\rho_b + \rho_t}. \tag{13}$$

2.6. Temperature and Water Vapor Fluctuations

From experimental observations by Niemela et al. (2000), the turbulent temperature fluctuation scale in single-phase RBC is given by

$$\frac{T'}{\Delta T} \propto Ra^{-1/7}. \tag{14}$$

Subsequently,

$$T' \propto H^{-3/7} \Delta T^{6/7}. \tag{15}$$

The temperature and water-vapor mixing ratio have slightly different diffusivities, which is only significant close to the boundaries. Consequently, it is reasonable to assume similar behavior for water-vapor as well. Therefore,

$$\frac{Q'_v}{\Delta Q_v} \propto Ra^{-1/7}. \tag{16}$$

Similar to Equation 15, for water vapor fluctuations we have

$$Q'_v \propto H^{-3/7} \Delta Q_v^{6/7}. \tag{17}$$

From Niemela et al. (2000), the proportionality constant of 0.37 fits the experimental temperature data. It should be noted that this constant for water vapor mixing ratio might be different.

From Equations 15 and 17, as the height of the chamber increases, the fluctuations of both temperature and water vapor decrease. Whereas, as the temperature or water vapor difference between the top and bottom surface increase, the corresponding fluctuations also increase. On the other hand, if the temperature and water vapor gradients are fixed, the fluctuations scale as $H^{-3/7}$.

For RBC Niemela et al. (2000) and Chillà and Schumacher (2012) demonstrated the scalar fluctuations to be approximately Gaussian distributed. Therefore, the temperature variance is of the form

$$\overline{T'^2} \propto H^{-6/7} \Delta T^{12/7}. \tag{18}$$

Table 1
Heights, Physical Dimensions, Number of Grid Boxes, Corresponding Rayleigh Numbers, and Aerosol Injection Rates for Convection–Cloud Chambers With a Temperature Difference of 14 K and a Mean Temperature of 283.14 K

H	Physical dimensions	# Grid boxes	Rayleigh number ($\times 10^9$)	Aerosol injection rate
1	$2 \times 2 \times 1$ m	64×64 x 32	1.38	1.56 cm^{-3} s^{-1}
2	$4 \times 4 \times 2$ m	128×128 x 64	11.06	0.8 cm^{-3} s^{-1}
4	$8 \times 8 \times 4$ m	256×256 x 128	88.51	0.5 cm^{-3} s^{-1}
8	$16 \times 16 \times 8$ m	512×512 x 256	708.1	–

Identically, the water vapor variance can be written as

$$\overline{Q_v'^2} \propto H^{-6/7}\,\Delta Q_v^{12/7}. \tag{19}$$

Kulmala et al. (1997) derived the supersaturation variance equation using Taylor expansions:

$$\overline{S'^2} \propto \overline{S}^2\left(\frac{\overline{Q_v'^2}}{\overline{Q_v}^2} - \frac{2L_w}{R_v\overline{T}}\frac{\overline{Q_v'T'}}{\overline{Q_v}\,\overline{T}} + \left(\frac{L}{R_v\overline{T}}\right)^2\frac{\overline{T'^2}}{\overline{T}^2}\right). \tag{20}$$

The co-variance term has been found to be close to unity (Chandrakar, Cantrell, et al., 2020; Thomas et al., 2021), hence $\overline{Q_v'T'}$ scales identical to temperature variance (Equation 18). From Equations 18–20, with the same boundary conditions, the supersaturation fluctuation variance has a height dependence given by

$$\overline{S'^2} \propto H^{-6/7}. \tag{21}$$

From Equation 21, the variance of supersaturation fluctuations is nearly inversely proportional with height.

3. Numerical Modeling

To study the turbulence and microphysical properties within the convection–cloud chamber, we have modified the System of Atmospheric Modeling (SAM, Khairoutdinov and Randall (2003)) with bin microphysics to simulate the turbulence and microphysical properties in the Pi chamber (Thomas et al., 2019, 2022; Yang et al., 2022).

The effect of scaling on microphysics is investigated using convection chambers for three different heights (1 m, 2 m, and 4 m). For the scaling of dynamics, an additional run with a height of 8 m is also investigated. The aspect ratio (i.e., width-to-height ratio) is maintained 2 to mitigate any weak dependence on the Nusselt and Reynolds numbers. For all the simulations, the grid box sizes are maintained at $3.125 \times 3.125 \times 3.125$ cm, and the time stepping at 0.02 s. Though it is computationally advantageous to increase the grid box size and time step as chamber size is increased, we retained the grid box size and time step used for the numerical simulation of the Pi Chamber (Thomas et al., 2019), for two reasons. First, this numerical setup has been validated for boundary fluxes, turbulence intensity, and large scale frequency against the experiments (Thomas et al., 2019). Second, this ameliorates any grid dependence of momentum or scalar fluxes at the top and bottom surfaces. For all cases, the temperature difference between the top and the bottom surfaces, ΔT, is 14 K and the mean temperature is 283.14 K. For fair comparison across the microphysics regimes (Chandrakar et al., 2016; Thomas et al., 2022), we ensure the number of droplets per unit volume is the same across different sized chambers. This is achieved by varying aerosol injection rates. The scaling and the implications of aerosol cycling is discussed in Section 4. Table 1 details the physical dimensions, number of grid boxes, and Rayleigh numbers for the four chambers that have been simulated. Please note that only the first three chamber sizes are used for microphysics inter-comparison.

The simulations are set up as follows. The top and bottom surfaces are, set to be 276.15 and 290.15 K, respectively, are independent of chamber size. Supersaturation in the chamber is reached by keeping both surfaces saturated with respect to water. A two-moment bin microphysics scheme based on Chen and Lamb (1994) is used to simulate cloud microphysical properties and processes (Yang et al., 2022). Specifically, monodisperse NaCl particles with a dry diameter of 125 nm are injected into the chamber at a constant rate. Injected dry aerosols are activated as cloud droplets if the environmental supersaturation is larger than the critical supersaturation of these aerosol particles based on the Köhler theory. Cloud droplets in each grid box are represented by 33 mass-doubling bins, starting from 1-μm radius. Newly activated cloud droplets are added in the first cloud bin (about 1 μm). Cloud droplets can grow by condensation and by collision coalescence, and finally fall out due to sedimentation. If cloud droplets are less than 1 μm in radius due to evaporation, they will become dry aerosol particles with a diameter of 125 nm and they can be activated as cloud droplets again when condition meets (i.e., environmental supersaturation is larger than the critical supersaturation). If the collision process is active, the collision kernel is parameterized based on Simmel et al. (2002) (Equation 13 therein). Terminal velocity

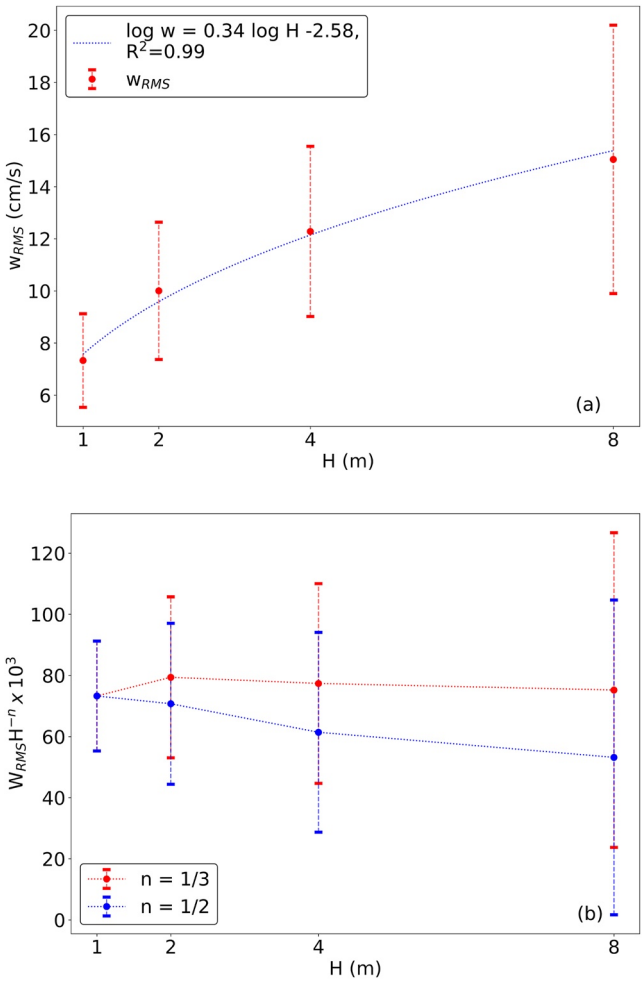

Figure 1. Top panel (a): RMS vertical velocity versus height of the simulated convection–cloud chambers; best-fit power law is also shown. Bottom panel (b): Compensated RMS vertical velocity plotted against the height of the chambers. The simulation results support the $H^{1/3}$ scaling suggested by Deardorff. For all simulations, the temperature difference between the top and the bottom plate is 14 K and the mean temperature is 283.14 K.

of the mean droplet size in each bin is calculated based on Beard (1976). Numerical algorithms for calculating cloud microphysical processes (i.e., growth by condensation and collision) are detailed in Chen (1992). In this study, we assume the sidewalls are adiabatic and cloud droplets cannot be absorbed by the sidewalls for simplification. Steady state can be reached when the formation of cloud droplets arising from a constant aerosol injection rate is balanced by the loss of cloud droplets due to sedimentation. An additional volumetric loss mechanism is also implemented to emulate sidewall losses, and prevent build up in the system. The aerosol injection rate, as shown in Table 1, is chosen differently in different chambers such that the cloud droplet number concentration in the steady state is the same (around 480 cm^{-3}). The time needed to reach a steady state is as fast as 20 min in the 1-m chamber, and as slow as 2 hr in the 4-m chamber. The results presented in the current study are obtained by averaging at least five instances of 3D outputs from the cloud chamber simulations at a steady state.

4. Results

In this section we first show results to validate the velocity and scalar variance scaling introduced in Section 2. We pay particular attention to the question of whether free-fall or Deardorff velocity scales are appropriate, which also determines the relevant scaling of the characteristic time. We then turn our attention to the microphysics. Specifically, we explore how aerosol injection rate and spatial distribution influence the microphysical properties. In the end, we explore the dependence of collision–coalescence growth on chamber size.

4.1. Scaling of Characteristic Velocity With Chamber Height

Figure 1 shows the root-mean-square (RMS) vertical velocity versus height of the simulated convection–cloud chambers. The velocities are averaged over the bulk fluid, defined as the region of the chamber at least $H/4$ away from each boundary, for at least 5 different time snapshots of the system while in the stationary state.

The top panel of Figure 1 includes a fit for the scaling of RMS vertical velocities obtained from 3D outputs of the LES simulations for different chamber sizes. The blue dotted line is the best linear fit in the log-log space and explains 99% of the variance of data. This best fit has a slope of 0.34, and is therefore consistent with 1/3-scaling predicted by Deardorff (Deardorff, 1970).The bottom panel of Figure 1 is the compensated vertical velocity plotted against height (i.e., normalized by prediction). Two different exponents are used for the compensation: 1/2 corresponding to the free fall velocity scale (Equation 6) and 1/3 corresponding to the Deardorff velocity scale (Equation 8). In the compensated plot, we expect a constant y-value for all heights if the scaling is perfect. It is evident that the exponent of 1/3 produces a much more satisfactory result than the 1/2 scaling. Therefore, the LES results support using Deardorff's expression for the characteristic vertical velocity scale, given by Equation 7. This, in turn, also implies that the characteristic time scale based on the Deardorff convective velocity, given by Equation 10, is the appropriate choice. For Rayleigh-Bénard convection with a constant imposed ΔT, the average heat flux is approximately constant. This is consistent with the Nusselt number scaling as Rayleigh number to the 1/3 power. We interpret the Deardorff velocity scale as the natural velocity scale derived from this constant heat flux, which is limited by the viscous boundary layer thickness (He & Xia, 2019). On the contrary, the free fall velocity scale assumes air parcels fall under the influence of gravity through the mixed layer height of the chamber and does not account for the presence of the boundary layer.

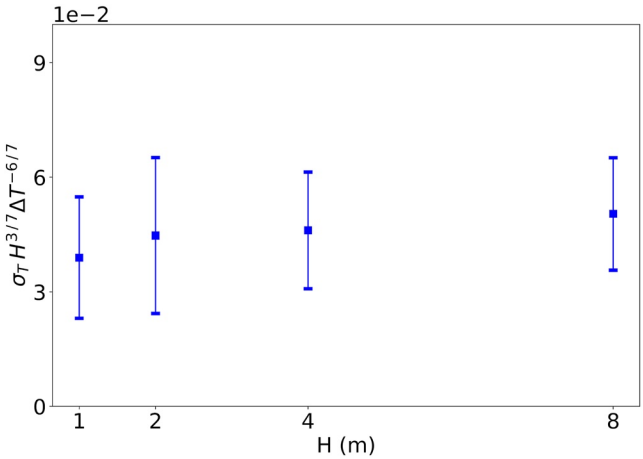

Figure 2. Compensated temperature fluctuations are plotted against the height of the chamber. The temperature difference between the top and the bottom plate is 14 K and the mean temperature is 283.14 K.

4.2. Scaling of Scalar Variability With Chamber Height

Figure 2 shows the compensated standard deviation of temperature (σ_T) plotted against height. The compensation uses the exponents of H and ΔT given by Equation 15. As in the previous sub-section, only the data from the bulk volume is plotted in Figure 2.The error bars for Figure 2 are the standard deviation of σ_T obtained from each of the 3D outputs at the stationary state. We note that the compensated value is constant within the statistical uncertainty corresponding to the given volume and time averaging. Please note, the intention is to show the relevant scaling than a specific value for the constant. This provides further support for the scaling given by Equation 15, as well as the related scalings for water vapor and supersaturation described in Section 2.6.

4.3. Scaling of Aerosol Properties With Chamber Height

Clouds are maintained in a convection–cloud chamber by introducing a steady source of aerosols to serve as cloud condensation nuclei (CCN). In this section we discuss how the aerosol injection rate influences microphysical properties. We first consider the rate of injection, and second, the spatial distribution of injection.

4.3.1. Scaling of Aerosol Injection Rate With Height to Maintain Similar Cloud Microphysical Properties

The rate of aerosol injection strongly influences the shape of the droplet size distribution, as well as the liquid water content, for the stationary state within a convection–cloud chamber (Chandrakar et al., 2016; Chandrakar, Saito, et al. 2020; Krueger, 2020). We consider the question, how well can the microphysical properties be matched as the scale of a convection–cloud chamber is increased? Previous studies show that with increasing aerosol injection rate, the cloud droplet size distribution becomes narrower, leading to an increase in cloud droplet number concentration and a decrease in the mean droplet size (Chandrakar et al., 2016; Thomas et al., 2019; Yang et al., 2022). In this study, we try to address the following questions: (a) can we match the droplet size distribution in convection cloud chambers of different sizes by changing the aerosol injection rates? (b) if the answer to (a) is yes, how does the aerosol injection rate scale with chamber height?

As shown in Figure 3, not only can the droplet number concentration be matched, but the shape of the droplet size distribution, and therefore the liquid water content (and other moments of the size distribution), can also be matched reasonably well. The most significant differences are in the smallest droplet-size bins, as a result of the changing influence of fluctuations on droplet activation (Prabhakaran et al., 2020). The smallest bin is depressed in cases with greatest H, and thus consistent with the fluctuation picture presented by Prabhakaran et al. (2020). In the simulations of convection chambers with three different heights (1, 2, and 4 m), the match in cloud microphysical properties is achieved by adjusting the aerosol injection rate to obtain identical droplet number concentrations (≈480 cm^{-3}). Specifically, the injection rate per unit volume for 1-m and 2-m chambers are 3.12 and 1.95 times that for a 4-m-high chamber. Thus, the injection rate per unit volume scales approximately inversely as the height of the cloud chamber. Viewed from a different perspective, the total injection rates for 2, and 4-m chambers are 5.0 and 20.5 times that of the 1-m case. The extensive injection rate increases approximately according to the cross-sectional area of the chamber. This can be understood from the fact that the number budget is a volumetric source balanced by sedimentation to the bottom surface of the chamber. Finally, we note that the reactivation of CCN is enabled in these simulations. Therefore, the relationship between injection rate and cloud-droplet number increases monotonically but with some nonlinearity due to the fact that the relative magnitude of the mean and fluctuating supersaturations

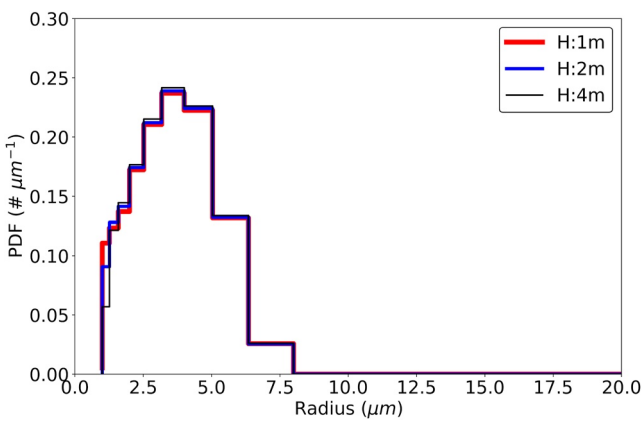

Figure 3. Cloud droplet size distributions for convection–cloud chambers of height 1, 2, and 4 m. The cloud droplet number (≈480 cm^{-3}) is matched for different sized chambers, and DSDs match reasonably well. The slight variation in the first bin is likely due to the role of turbulence in activation. The temperature difference is 14 K and the mean temperature is 283.14 K. The aerosols are injected uniformly throughout the volume.

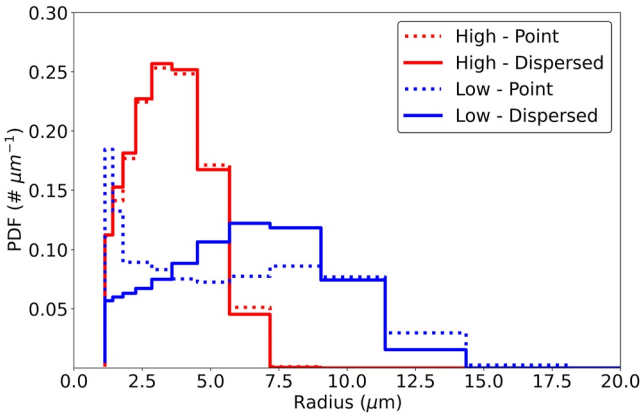

Figure 4. Cloud droplet size distributions for point (dotted lines) and dispersed (solid lines) aerosol injection in a convection–cloud chamber of height 1 m. The high droplet number (≈960 cm^{-3}) and low droplet number (≈60 cm^{-3}) cases are shown in red and blue respectively. The temperature difference is 14 K and the mean temperature is 283.14 K.

change, thereby changing the rates of activation and deactivation of CCN (Prabhakaran et al., 2020). In practice, the cloud droplet number concentrations for different chamber heights are matched by trial and error.

4.3.2. Single-Point Versus Volume-Dispersed Injection of Aerosol

Although it is not strictly related to scaling, we use the current simulation as an opportunity to qualitatively illustrate the impact of localized single-point injection on droplet size distribution, in contrast with a homogeneous, volume-dispersed injection of aerosol. From a modeling perspective, the latter is more convenient and numerically stable (as done in Yang et al. (2022) and all simulations above), but the former is conceptually closer to real experiments. For this study, a convection–cloud chamber of $H = 1$ m, with $\Delta T = 14$ K is simulated for point and volume-dispersed aerosol injection. For the point injection, aerosol is injected at the exact center of the chamber ($x = 1$ m, $y = 1$ m, $z = 0.5$ m) and in both cases, the droplet number concentration is 60 cm^{-3}. The thermodynamic boundary conditions and the total number of droplets per unit volume of the chamber are kept constant across both injection cases. We investigate how different injection regions affect the stationary state droplet size distributions.

From Figure 4, we see that at low total aerosol injection rate, the droplet size distribution for point injection is broader than the uniform dispersed injection case. The spatial variability in the droplet number for low cloud droplet number cases is due to droplet transport via advection and gravitational settling, and variability in the supersaturation field. We can see droplets of diameters as large as 30 μm. These large droplets are due to a combination of large mean supersaturation (Krueger, 2020) and turbulent fluctuations (Chandrakar et al., 2016).

Irrespective of the spatial pattern of aerosol injection, the droplet size distributions are nearly the same in the polluted conditions. At high aerosol injection rates, unactivated CCN are present abundantly, thereby acting as a sink for any localized supersaturation fluctuations. The presence of a uniformly-distributed buffer throughout the volume of the chamber negates any effect that spatial or temporal variability might have had. At low aerosol injection rate, it is interesting to see that the distribution is bimodal for point aerosol injection, while it is single-mode for dispersed aerosol injection. It should be mentioned that, although the bimodal distribution is qualitatively similar to the observation, the smaller mode at around 1 μm in Figure 4 are still cloud droplets, not haze particles as in Prabhakaran et al. (2020). More efforts are needed to properly resolve the submicron haze particles and the associated activation and deactivation processes in the simulation, which is out of the scope of this study. For now, we note that when we remove the grid boxes surrounding the point injection grid box and plot the droplet size distributions, the small mode corresponding to newly-activated droplets becomes less prominent and only the main mode remains. The mode essentially disappears within one large eddy length scale (several 10s of cm).

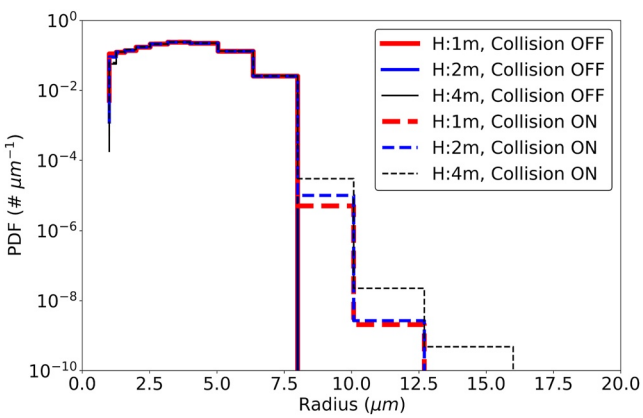

Figure 5. Cloud DSDs for height 1m (red), 2m (blue), and 4m (black) with collision turned off (line) and collision turned on (dashed). The temperature difference between the top and the bottom surface is 14 K. The injection rates are adjusted to produce 480 droplets per cm^3 for all chambers.

4.4. Scaling of Collisional Growth With Chamber Height

We conclude our investigation of scaling by exploring the role of droplet growth by collision–coalescence, and how it scales with the height of a convection–cloud chamber. To do this, we use the same aerosol injection rates that led to matching of the droplet size distributions with varying chamber size (as shown in Figure 3). We then run the simulation with collisional growth turned on and compare to the runs with condensation growth only. Figure 5 illustrates the cloud droplet size distributions (DSDs) for chambers of heights 1 m, 2 m, and 4 m with and without collision coalescence in the steady state. The cloud droplet number concentration is maintained at ≈480 cm^{-3} for all chamber sizes. The mean supersaturation in the stationary state decreases with H. DSDs are generated by averaging spatially over the bulk of the chamber and temporally across at least five instances from the quasi-stationary cloud regime. The 3D outputs are separated temporally

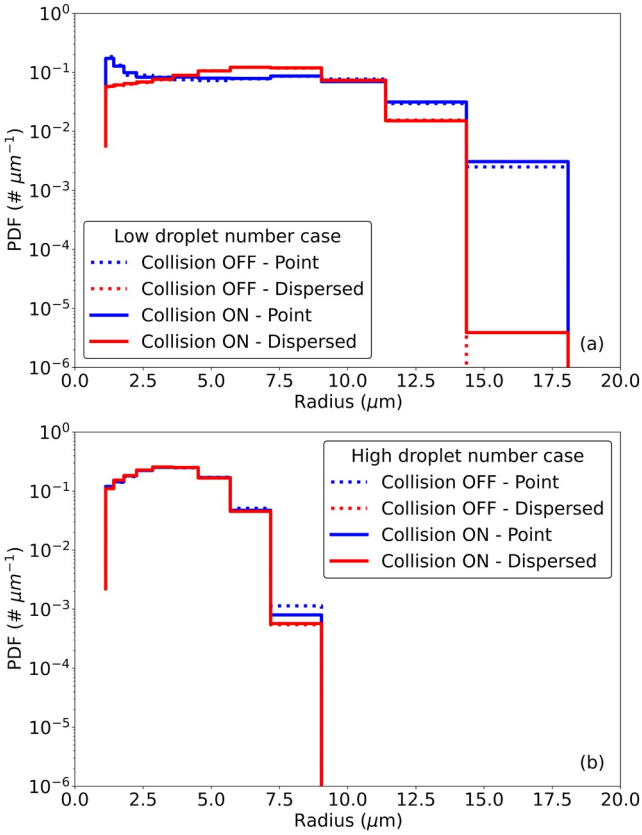

Figure 6. Top panel (a): DSD of low droplet number case (≈60 cm^{-3}) for cases with point and dispersed injections with collision turned on and off. Bottom panel (b): DSD of high droplet number case(≈960 cm^{-3}) for cases with point and dispersed injections with collisions turned on and off. The temperature difference is 14 K and the mean temperature is 283.14 K.

by 5 min. The sampling distance is chosen to avoid any wall effects, and the sampling time is chosen to avoid any correlation effects due to turbulence (Anderson et al., 2021; Niedermeier et al., 2018). At least 3.68×10^5, 1.47×10^6, and 4.92×10^8 grid boxes have been sampled for 1-m, 2-m and 4-m chambers, respectively to produce the PDFs.

The distributions shown in Figure 5 include those previously shown in Figure 3, but with a larger radius range and a logarithmic *y*-axis so as to reveal changes in the right tails of the distributions. Again, we see that for cases with collision turned off the cloud DSDs for 1-m, 2-m, and 4-m chambers shown by the red, blue, and black solid lines overlap each other. The condensational growth of the droplets is governed by the supersaturation, the lifetime of the droplets dictated by the height of the chamber, and the presence of excess CCN.

In contrast, with collisional growth turned on, cloud DSDs are starkly different. The DSDs for the 4-m chamber are broader, and have higher concentrations of large droplets than the corresponding 2-m and 1-m cases. Even though the 2-m case occupies the same number of bins as the 1-m case, there is a relative increase in the number of large droplets. The broadening and increasing magnitude of the large-droplet tail of the DSD with chamber height is consistent with the increase of the chamber height relative to the collision mean-free path, which remains constant because of the fixed number concentration and liquid water content. The ratio of the mean free path and the chamber height (the Knudsen number for droplet collisions) decreases by a factor of 4 for the 4-m chamber compared to the 1-m chamber, thereby increasing the relative role of collisional growth. In other words, large droplets in the 4-m chamber have longer lifetimes and a significant increase in path length traveled before they sediment to the bottom, during which time they encounter 4 times more droplets, on average, than the 1-m case (Kostinski & Shaw, 2005). These effects can be directly identified and disentangled using lifetime analysis done by MacMillan et al. (2022), which requires the use of Lagrangian microphysics approaches.

Finally, for completeness we show results for the influence of the spatial form of point versus distributed aerosol injection on collision broadening. In each of the cases with collision on and off, the droplet number concentration is 60 cm^{-3}. Again, the calculation is performed only for $H = 1$ m. Figure 6 shows the same distributions as in Figure 4, but now with distributions with collisional growth turned on. There is a slight broadening of the distribution by collisions, but in the clean case the broadening due to changing the spatial distribution of aerosol injection is more significant.

5. Concluding Remarks

This study uses a combination of previously determined scale relations from the turbulent Rayleigh-Bénard convection community, and large eddy simulation with bin cloud microphysics to validate and explore the effects of scaling the size of experimental convection–cloud chambers. For moist Rayleigh-Bénard convection, two important non-dimensional numbers relevant to turbulence and cloud formation are *Ra* and *Nu*. By increasing the characteristic length scale, the chamber height *H*, *Ra* scales as H^3, whereas *Nu* scales as *H*. The flux from the boundary is approximately independent of *H*. The characteristic velocity follows Deardorff scaling in the bulk, and is validated by the LES studies as shown in Figure 1. Consequently, the system time scales as $H^{2/3}$. The Damkoehler number ($\propto \tau$) therefore has a height dependence because of the increase of τ with *H*. For the same thermodynamic boundary conditions, and same microphysical conditions, a larger chamber therefore has a larger Damkoehler number. Subsequently, the Rouse (or sedimentation) number *Rou* given by w_T/w, will have a chamber-height dependence through the characteristic velocity *w*. Therefore, *Rou* scales as $H^{-1/3}$ and we can expect that the size distribution will be well mixed within the convection chamber up to larger particle diameters (Bragg et al., 2021; Park et al., 2018), and that mean residence times will be longer.

From Equation 13 it is clear that the steady state mean temperature, mean water vapor mixing ratio, and mean supersaturation are independent of the chamber height. However, the temperature, water vapor, and supersaturation fluctuations decrease approximately as $H^{-3/7}$, for a fixed ΔT. Consequently, the relative dispersion for supersaturation $\sigma_s/\overline{s}$ also scales as $H^{-3/7}$. The variability of the fluctuation of temperature against height is also demonstrated in Figure 2.

The LES model is used to compare the effect of height on the collision–coalescence problem. For a fair comparison of microphysics across different heights of the chamber, an important question is whether it is possible to maintain identical microphysical properties, that is, fixed LWC and DSD shape as H is increased. In Figure 3 it is demonstrated that droplet size distributions for different chamber sizes indeed can be approximately matched, albeit with some deviation at the small droplet sizes. The droplet number concentrations are matched by adjusting the aerosol injection rates; roughly, the adjustment shows that the full-volume injection rate scales as the cross-sectional area of the chamber. We find that holding the number of cloud droplets per unit volume to be a constant leads to a similar size distribution shape as the chamber size is varied, when only condensation growth is accounted for. This, in turn, implies that the collision mean-free-path remains constant. However, as seen in Figure 5, the droplet size distribution shows a broader large-droplet tail when collision–coalescence growth is included in the LES, and this tail increases in magnitude and extends to larger droplet sizes as the chamber height is increased.

How does the collision probability vary as the height of a convection-cloud chamber is increased, while holding the droplet size distribution shape and concentration constant? Intuitively, we can anticipate that the collision growth is proportional to the "swept volume" of a falling collector drop, and therefore should scale with increasing H. Expressed differently, we can expect that the Knudsen number $Kn = \lambda/H$ will decrease if the mean free path λ is only a function of microphysical properties (e.g., for a "frozen flow" with no turbulence contributions). Furthermore, for $H \ll \lambda$, the probability of collision will scale as $Kn^{-1} = H/\lambda$. The mean distance traveled by a falling drop of radius r_2, to collide with a droplet of radius r_1, in the laboratory reference frame is

$$\lambda = kr_2^2\left[n_1\pi(r_1 + r_2)^2 k|r_2^2 - r_1^2|\epsilon(r_1, r_2)\right]^{-1}, \tag{22}$$

where n_1 is the number concentration of droplets of size r_1, k is a constant for Stokes terminal fall speed $v_T = kr^2$, and ϵ is the collision efficiency (coalescence efficiency is assumed to be 1). The efficiency ϵ is poorly known for droplet radii in the range 1–10 μm, so we take it to be a constant 0.1 for the purposes of this calculation. If we interpret H/λ as a collision probability, then it follows that total probability of collision scales linearly with H. We illustrate the point using the $H = 2$ m size distributions shown in Figure 5. Using the observed concentration and radii of the bins, we can sum over all bins to obtain the total probability of collision during the lifetime of a collector drop of radius r_j: $\sum_i H/\lambda_{i,j}$. For the largest radius bin observed in the collision-off DSD, the probability is approximately 0.2. Considering the large-droplet tail that appears in the collision-on case, the first bin corresponding to radii from 8.0 to 10.1 μm the probability increases to 0.4. For the second bin in the collision-growth tail, from 10.1 to 12.7 μm, the probability reaches unity. Therefore, for the conditions of this simulation, condensation brings the system just to the verge of coalescence, and the appearance of larger drops through coalescence gets the collisional-growth process going efficiently (limited, however, by the lifetime of a collector drop in the chamber). This helps to explain why increasing H by a factor of 2 leads to a nearly proportional increase in the concentrations within the largest size bins populated by collisional growth. Exploring the collision-growth behavior over a range of microphysical conditions is the subject of ongoing research.

Primary motivations for developing a convection–cloud chamber with larger H are to achieve longer residence times relevant to aerosol processing in clouds and the onset of growth by collision–coalescence, and to achieve longer Lagrangian correlation times for supersaturation fluctuations relevant to droplet growth by condensation. How can the current findings help guide future computational and experimental studies of these processes? First, we can ask whether there is enough collisional growth to be observed experimentally. How much collisional growth is enough, however, is largely a question of measurement technology. The simulations presented here are a first step toward answering this important question, by demonstrating the quantitative growth of the large-droplet tail with increasing chamber height. Second, what are the implications for research on stochastic condensation? The change in magnitude of fluctuations compared to mean supersaturation, with increasing H, tends to shift the droplet growth to the mean-dominated regime, as defined by Prabhakaran et al. (2020, 2022). However, increasing the droplet concentration will tend to shift the system to regimes where fluctuations play a more significant

role, thereby providing a straightforward approach for exploring all three growth regimes. Third, what are the implications for the spatial pattern of aerosol injection, and could this mask signatures of collisional growth? The results presented here demonstrate that we have the simulation capability of representing non-uniform injection, and that this can be an important consideration in relatively clean conditions. Furthermore, the observed bimodality is a local phenomenon near the point of injection, so there are implications for the location of droplet sampling. Observations from the Pi chamber (Chandrakar et al., 2016, 2018; Desai et al., 2018) are conducted away from the point of injection, where the activation droplet bin mode is absent. It has been shown in prior work, using a variety of modeling approaches, that for condensation growth there is reasonable agreement with simulations, with the largest uncertainty being the representation of sidewall boundary conditions (Xue et al., 2022). A detailed exploration of the sidewall boundary conditions and challenges in accurate characterization and modeling can be found in Thomas et al. (2019) and Anderson et al. (2021). The degree to which the presence of a smaller, activation mode might enhance the collision-coalescence is a topic that will need further investigation.

One motivation for understanding the scaling of turbulence, thermodynamics and microphysics within a convection–cloud chamber is to consider how the accessible region of dimensionless parameter space can be modified through changes in system height H. This is relevant both to laboratory chambers and direct numerical simulations. The results presented here show the general trends and are an initial step toward understanding the detailed behavior. The parameter space is multi-dimensional and LES with microphysics is computationally expensive, so a thorough exploration will require a combination of more computational resources and more idealized and efficient analytical or computational methods. In particular, one-dimensional turbulence approaches and collision models are likely to be beneficial (Chandrakar et al., 2020; Krueger & Kerstein, 2018). At this stage, it is clear that increasing the size of a convection–cloud chamber allows larger Da and smaller Rou and Kn to be explored, in addition to larger Ra and Nu. All of these trends likely bring laboratory and direct-simulation tools closer to the microphysical dimensionless space occupied by real clouds. We anticipate that similar models will be useful for scaling of microphysical and turbulence properties within turbulent, cloudy mixed-layers in the atmosphere, such as in fogs.

Data Availability Statement

The SAM LES is available from Marat Khairoutdinov of Stony Brook University: http://rossby.msrc.sunysb.edu/~marat/SAM.html. Model output for generating the results shown in the figures is available at: https://digitalcommons.mtu.edu/all-datasets/36/.

Acknowledgments
This research was supported by U.S. National Science Foundation Grant AGS-2133229. This study was also supported by the U.S. Department of Energy Office of Science Biological and Environmental Research as part of the Atmospheric Systems Research (ASR) Program. Brookhaven National Laboratory is operated by Battelle for the U.S. Department of Energy under contract DE-SC00112704. The Pacific Northwest National Laboratory is operated by Battelle for the U.S. Department of Energy under Contract DE-AC05-76RL01830. Portage and Superior, high-performance computing systems at Michigan Technological University, were used in obtaining results presented in this publication. The authors thank S. Gowtham for assistance with the HPC implementation.

References

Anderson, J. C., Thomas, S., Prabhakaran, P., Shaw, R. A., & Cantrell, W. (2021). Effects of the large-scale circulation on temperature and water vapor distributions in the π chamber. *Atmospheric Measurement Techniques*, *14*(8), 5473–5485. https://doi.org/10.5194/amt-14-5473-2021

Beard, K. V. (1976). Terminal velocity and shape of cloud and precipitation drops aloft. *Journal of the Atmospheric Sciences*, *33*(5), 851–864. https://doi.org/10.1175/1520-0469(1976)033<0851:tvasoc>2.0.co;2

Bhandari, J., China, S., Chandrakar, K. K., Kinney, G., Cantrell, W., Shaw, R. A., et al. (2019). Extensive soot compaction by cloud processing from laboratory and field observations. *Scientific Reports*, *9*(1), 1–12. https://doi.org/10.1038/s41598-019-48143-y

Bragg, A. D., Richter, D. H., & Wang, G. (2021). Mechanisms governing the settling velocities and spatial distributions of inertial particles in wall-bounded turbulence. *Physical Review Fluids*, *6*, 064302. https://doi.org/10.1103/PhysRevFluids.6.064302

Chandrakar, K. K., Cantrell, W., Chang, K., Ciochetto, D., Niedermeier, D., Ovchinnikov, M., et al. (2016). Aerosol indirect effect from turbulence-induced broadening of cloud-droplet size distributions. *Proceedings of the National Academy of Sciences*, *113*(50), 14243–14248. https://doi.org/10.1073/pnas.1612686113

Chandrakar, K. K., Cantrell, W., Kostinski, A., & Shaw, R. (2018). Dispersion aerosol indirect effect in turbulent clouds: Laboratory measurements of effective radius. *Geophysical Research Letters*, *45*(19), 10–738. https://doi.org/10.1029/2018gl079194

Chandrakar, K. K., Cantrell, W., Krueger, S., Shaw, R. A., & Wunsch, S. (2020). Supersaturation fluctuations in moist turbulent Rayleigh–Bénard convection: A two-scalar transport problem. *Journal of Fluid Mechanics*, *884*, A19. https://doi.org/10.1017/jfm.2019.895

Chandrakar, K. K., Saito, I., Yang, F., Cantrell, W., Gotoh, T., & Shaw, R. A. (2020). Droplet size distributions in turbulent clouds: Experimental evaluation of theoretical distributions. *Quarterly Journal of the Royal Meteorological Society*, *146*(726), 483–504. https://doi.org/10.1002/qj.3692

Chang, K., Bench, J., Brege, M., Cantrell, W., Chandrakar, K., Ciochetto, D., et al. (2016). A laboratory facility to study gas–aerosol–cloud interactions in a turbulent environment: The π chamber. *Bulletin of the American Meteorological Society*, *97*(12), 2343–2358. https://doi.org/10.1175/bams-d-15-00203.1

Chen, J.-P. (1992). *Numerical simulations on the redistribution of atmospheric trace chemicals through cloud processes*. PhD thesis. The Pennsylvania State University.

Chen, J.-P., & Lamb, D. (1994). Simulation of cloud microphysical and chemical processes using a multicomponent framework. Part I: Description of the microphysical model. *Journal of the Atmospheric Sciences*, *51*(18), 2613–2630. https://doi.org/10.1175/1520-0469(1994)051<2613:socmac>2.0.co;2

Chillà, F., & Schumacher, J. (2012). New perspectives in turbulent Rayleigh-Bénard convection. *The European Physical Journal E*, *35*(7), 58. https://doi.org/10.1140/epje/i2012-12058-1

Cooper, W. A. (1989). Effects of variable droplet growth histories on droplet size distributions. Part I: Theory. *Journal of the Atmospheric Sciences*, *46*(10), 1301–1311. https://doi.org/10.1175/1520-0469(1989)046<1301:eovdgh>2.0.co;2

Deardorff, J. W. (1970). Convective velocity and temperature scales for the unstable planetary boundary layer and for Rayleigh convection. *Journal of the Atmospheric Sciences*, *27*(8), 1211–1213. https://doi.org/10.1175/1520-0469(1970)027<1211:cvatsf>2.0.co;2

Desai, N., Chandrakar, K., Chang, K., Cantrell, W., & Shaw, R. (2018). Influence of microphysical variability on stochastic condensation in a turbulent laboratory cloud. *Journal of the Atmospheric Sciences*, *75*(1), 189–201. https://doi.org/10.1175/jas-d-17-0158.1

Desai, N., Chandrakar, K., Kinney, G., Cantrell, W., & Shaw, R. (2019). Aerosol-mediated glaciation of mixed-phase clouds: Steady-state laboratory measurements. *Geophysical Research Letters*, *46*(15), 9154–9162. https://doi.org/10.1029/2019gl083503

Hartmann, R., Chong, K. L., Stevens, R. J., Verzicco, R., & Lohse, D. (2021). Heat transport enhancement in confined Rayleigh-Bénard convection feels the shape of the container. *Europhysics Letters*, *135*(2), 24004. https://doi.org/10.1209/0295-5075/ac19ed

He, Y.-H., & Xia, K.-Q. (2019). Temperature fluctuation profiles in turbulent thermal convection: A logarithmic dependence versus a power-law dependence. *Physical Review Letters*, *122*(1), 014503. https://doi.org/10.1103/physrevlett.122.014503

Iyer, K. P., Scheel, J. D., Schumacher, J., & Sreenivasan, K. R. (2020). Classical 1/3 scaling of convection holds up to $Ra = 10^{15}$. *Proceedings of the National Academy of Sciences*, *117*(14), 7594–7598. https://doi.org/10.1073/pnas.1922794117

Kang, L., Marchand, R., Wood, R., & McCoy, I. L. (2022). Coalescence scavenging drives droplet number concentration in southern ocean low clouds. *Geophysical Research Letters*, *49*(7), e2022GL097819. https://doi.org/10.1029/2022gl097819

Khairoutdinov, M. F., & Randall, D. A. (2003). Cloud resolving modeling of the ARM summer 1997 IOP: Model formulation, results, uncertainties, and sensitivities. *Journal of the Atmospheric Sciences*, *60*(4), 607–625. https://doi.org/10.1175/1520-0469(2003)060<0607:crmota>2.0.co;2

Kostinski, A. B., & Shaw, R. A. (2005). Fluctuations and luck in droplet growth by coalescence. *Bulletin of the American Meteorological Society*, *86*(2), 235–244. https://doi.org/10.1175/bams-86-2-235

Krueger, S. K. (2020). Equilibrium droplet size distributions in a turbulent cloud chamber with uniform supersaturation. *Atmospheric Chemistry and Physics*, *20*(13), 7895–7909. https://doi.org/10.5194/acp-20-7895-2020

Krueger, S. K., & Kerstein, A. R. (2018). An economical model for simulating turbulence enhancement of droplet collisions and coalescence. *Journal of Advances in Modeling Earth Systems*, *10*(8), 1858–1881. https://doi.org/10.1029/2017ms001240

Kulmala, M., Rannik, Ü., Zapadinsky, E. L., & Clement, C. F. (1997). The effect of saturation fluctuations on droplet growth. *Journal of Aerosol Science*, *28*(8), 1395–1409. https://doi.org/10.1016/s0021-8502(97)00015-3

MacMillan, T., Shaw, R. A., Cantrell, W. H., & Richter, D. H. (2022). Direct numerical simulation of turbulence and microphysics in the pi chamber. *Physical Review Fluids*, *7*(2), 020501. https://doi.org/10.1103/PhysRevFluids.7.020501

Niedermeier, D., Chang, K., Cantrell, W., Chandrakar, K. K., Ciochetto, D., & Shaw, R. A. (2018). Observation of a link between energy dissipation rate and oscillation frequency of the large-scale circulation in dry and moist Rayleigh-Bénard turbulence. *Physical Review Fluids*, *3*(8), 083501. https://doi.org/10.1103/physrevfluids.3.083501

Niemela, J., Skrbek, L., Sreenivasan, K., & Donnelly, R. (2000). Turbulent convection at very high Rayleigh numbers. *Nature*, *404*(6780), 837–840. https://doi.org/10.1038/35009036

Park, H. J., O'Keefe, K., & Richter, D. H. (2018). Rayleigh-Bénard turbulence modified by two-way coupled inertial, nonisothermal particles. *Physical Review Fluids*, *3*, 034307. https://doi.org/10.1103/PhysRevFluids.3.034307

Prabhakaran, P., Shawon, A. S. M., Kinney, G., Thomas, S., Cantrell, W., & Shaw, R. A. (2020). The role of turbulent fluctuations in aerosol activation and cloud formation. *Proceedings of the National Academy of Sciences*, *117*(29), 16831–16838. https://doi.org/10.1073/pnas.2006426117

Prabhakaran, P., Thomas, S., Cantrell, W., Shaw, R. A., & Yang, F. (2022). Sources of stochasticity in the growth of cloud droplets: Supersaturation fluctuations versus turbulent transport. *Journal of the Atmospheric Sciences*, *79*(12), 3145–3162. https://doi.org/10.1175/JAS-D-22-0051.1

Shaw, R. A., Cantrell, W., Chen, S., Chuang, P., Donahue, N., Feingold, G., et al. (2020). Cloud–aerosol–turbulence interactions: Science priorities and concepts for a large-scale laboratory facility. *Bulletin of the American Meteorological Society*, *101*(7), E1026–E1035. https://doi.org/10.1175/BAMS-D-20-0009.1

Shawon, A. S. M., Prabhakaran, P., Kinney, G., Shaw, R. A., & Cantrell, W. (2021). Dependence of aerosol-droplet partitioning on turbulence in a laboratory cloud. *Journal of Geophysical Research: Atmospheres*, *126*(5), e2020JD033799. https://doi.org/10.1029/2020jd033799

Simmel, M., Trautmann, T., & Tetzlaff, G. (2002). Numerical solution of the stochastic collection equation—Comparison of the linear discrete method with other methods. *Atmospheric Research*, *61*(2), 135–148. https://doi.org/10.1016/s0169-8095(01)00131-4

Thomas, S., Ovchinnikov, M., Yang, F., van der Voort, D., Cantrell, W., Krueger, S. K., & Shaw, R. A. (2019). Scaling of an atmospheric model to simulate turbulence and cloud microphysics in the pi chamber. *Journal of Advances in Modeling Earth Systems*, *11*(7), 1981–1994. https://doi.org/10.1029/2019ms001670

Thomas, S., Prabhakaran, P., Cantrell, W., & Shaw, R. A. (2021). Is the water vapor supersaturation distribution Gaussian? *Journal of the Atmospheric Sciences*, *78*(8), 2385–2395. https://doi.org/10.1175/jas-d-20-0388.1

Thomas, S., Prabhakaran, P., Yang, F., Cantrell, W. H., & Shaw, R. A. (2022). Dimensionless parameters for cloudy Rayleigh-Bénard convection: Supersaturation, Damköhler, and Nusselt numbers. *Physical Review Fluids*, *7*(1), 010503. https://doi.org/10.1103/PhysRevFluids.7.010503

Vallis, G. K., Parker, D. J., & Tobias, S. M. (2019). A simple system for moist convection: The rainy–bénard model. *Journal of Fluid Mechanics*, *862*, 162–199. https://doi.org/10.1017/jfm.2018.954

Xue, L., Bera, S., Chen, S., Choudhary, H., Dixit, S., Grabowski, W. W., et al. (2022). Progress and challenges in modeling dynamics–microphysics interactions: From the pi chamber to monsoon convection. *Bulletin of the American Meteorological Society*, *103*(5), E1413–E1420. https://doi.org/10.1175/bams-d-22-0018.1

Yang, F., Ovchinnikov, M., Thomas, S., Khain, A., McGraw, R., Shaw, R. A., & Vogelmann, A. M. (2022). Large-eddy simulations of a convection cloud chamber sensitivity to bin microphysics and advection. *Journal of Advances in Modeling Earth Systems*, *14*(5), e2021MS002895. https://doi.org/10.1029/2021ms002895

Zhang, L., Chong, K. L., & Xia, K.-Q. (2019). Moisture transfer by turbulent natural convection. *Journal of Fluid Mechanics*, *874*, 1041–1056. https://doi.org/10.1017/jfm.2019.463